

Low energy band structure in Bernal stacked hexlayer graphene: Landau fan diagram and resistance ridge

Tomoaki Nakasuga¹, Shingo Tajima¹, Taiki Hirahara¹, Ryoya Ebisuoka¹, Takushi Oka¹, Kenji Watanabe², Takashi Taniguchi² and Ryuta Yagi^{1*}

¹Graduate School of Advanced Sciences of Matter, Hiroshima University,
Kagamiyama 1-3-1, Higashi-Hiroshima, Hiroshima 739-8530, Japan

²National Institute for Materials Science (NIMS), Namiki 1-1, Tsukuba, Ibaraki,
305-0044 Japan.

(PACS 73.22.Pr, 73.61.-r, 73.50.Jt, 73.63.-b)

Abstract

The low-energy band structure of Bernal-stacked hexlayer graphene was investigated by the measuring transport properties of high-mobility graphene samples equipped with a top and a bottom gate electrode at low temperature and in a magnetic field. By analyzing the Landau fan diagram, it was found that the hexlayer graphene consisted of three different bilayer-like bands that overlap and form a semimetal. The electronic band structure was significantly influenced by the perpendicular electric field generated by the top and bottom gate voltages. The Landau fan diagram shows splitting of zero-mode Landau levels, while also the top and bottom gate voltage dependence of the resistivity at zero magnetic field shows ridge-like structure, similar to the one recently found in tetralayer graphene. It is shown that the ridge structure originates from the band structure of the Bernal-stacked hexlayer graphene. Most of the ridges originate from the bottoms of the bilayer-like bands, and a few ridges originate from the energy gap structures which locally close due to trigonal warping and expected to form mini-Dirac cones.

* Corresponding Author yagi@hiroshima-u.ac.jp

Introduction

Graphene is a two-dimensional material in the form of a honeycomb lattice of carbon atoms. It can be made by cleaving bulk crystal of graphite with adhesive tape [1]. Monolayer graphene is a gap-less semiconductor; the conduction band and valence band touch at the so-called Dirac point [2-3]. The Fermi velocity of graphene is comparable to those of metals, although the carrier density is much lower than those of the metals, which is due to the linear dispersion relation of the massless Dirac fermions. One of the most interesting features of graphene is that it is a potential material with which one can study the fundamental question of how atomic layers acquire a bulk nature as the number of layers increases. Indeed, graphene is expected to have totally different band structures depending on the number of layers and stacking [4-11]. Electrons in bilayer graphene behave as a two-dimensional gas of massive Dirac fermions, whose low-energy dispersion relation is approximated by a parabolic band. Trilayer graphene, on the other hand, has a bilayer-like band in addition to a monolayer-like band. The electronic band structure of graphene becomes more complicated as the number of layers increases; however, AB-stacked graphene shows a parity effect with respect to the number of layers [4-9]: in the case of an even number of layers, *i.e.*, $2n$ ($n = 1, 2, 3 \dots$), the electronic band structure consists of n bilayer-like bands, and in the case of an odd number of layers, *i.e.*, $2n + 1$ ($n = 1, 2, 3 \dots$), it consists of a monolayer-like band and n bilayer-like bands. Although the band structure in the high-energy regime was studied by using optical methods at the beginning of graphene research [12-19], the low-energy band structure remained less understood. It can be studied by observing the Shubnikov de-Haas (S-dH) effect, although it requires high-mobility samples in order to observe clear oscillations in magnetoresistance. To date, the Landau level structures of trilayer [20-24] and tetralayer graphene [24-29] have been studied in detail. Recently, we reported how the Landau level structure evolves in one- to seven-layer graphene [24].

From the studies of multilayer graphene, it has been recognized that the electronic band structure is influenced by the electrostatic potential arising from perpendicular electric fields due to the gate voltages [21,24,28,30-32]. In order to tune the static potential, samples with top and bottom gate electrodes were employed. Perpendicular electric fields open an energy gap [17,33-38], which results in bilayer graphene having insulating behavior [34]. In trilayer graphene,

although an energy gap appears at the bottom of the bilayer band, the density of states arising from the extra monolayer prevents it from having insulating behavior [37,39-42].

Recently investigations of the response of the band structure to a perpendicular electric field uncovered a new feature of multilayer graphene. AB-stacked tetralayer graphene showed resistance ridges in the top and bottom gate voltage dependence at zero magnetic field [28-29]; these ridges originate from the band structure. Moreover, we have found that resistance ridges are commonly observed in AB-stacked multilayer graphene, as we briefly reported for AB-stacked hexlayer graphene in Ref. [29].

In this paper, we study the low-energy band structure of AB-stacked hexlayer graphene. AB-stacked hexlayer graphene is expected to have three sets of bilayer-like bands as shown schematically in Fig. 1 (a). By measuring the Landau fan diagram in the presence and absence of perpendicular electric fields, we show that this picture is oversimplified. On the basis of the band structure, we also study the resistance ridge structures appearing in the top and bottom gate voltage dependence. Since AB-stacked hexlayer graphene has the least number of layers that would give three sets of bilayer-like bands, studying it enables us to investigate the origin of the resistance ridges, and show that they stem from the complicated band structure of AB-stacked hexlayer graphene.

Experimental

Our sample consisted of graphene encapsulated with thin *h*-BN flakes, on which were formed top and bottom gate electrodes. Flakes of graphene and *h*-BN were prepared by mechanical exfoliation of high-quality bulk crystals. An optical micrograph of the sample and a schematic diagram of the sample structure are shown in Figure 1 (b) and (c). A flake of moderately thick graphene, which was transferred onto the top of the stacks, served as a top gate electrode. The SiO₂ substrate, which was heavily doped and conducting at low temperature, served as a back gate electrode. Electrical contacts with encapsulated AB-stacked hexlayer graphene were formed using the edge contact technique [43]. Electrical contacts

with graphene serving as the top gate were formed at positions on the substrate where the encapsulated AB-stacked hexlayer graphene was absent.

Identifications of the number of layers and stacking are one of the most important points in this study. The number of layers was identified by combining information of on the optical contrast in the graphene image, atomic force microscopy (AFM), and the shape of the G' band of the Raman spectra. The stacking was verified by examining the shape of the Raman G' band and the structure of the Landau fan diagram [24] (see Appendix 2 for details).

The magnetoresistance measurements were performed at $T = 4.2$ K. Magnetic fields were applied using a superconducting solenoid. The resistivity measurements were done using the standard lock-in technique.

Results

Resistivity at zero magnetic field

Backgate voltage dependence of resistivity exhibited a significant dependence on the top gate voltage as shown in Fig. 2 (a). The resistivity traces show conspicuous peak structures, which are due to the charge neutrality. The peak resistivity increases with increasing $|V_t|$, which is relevant to the perpendicular electric field. Similar insulating behavior has been observed in bilayer graphene [34,40-41], and it is apparently different from that of AB-stacked trilayers, which show the opposite behavior [40-41]. Besides the large peak, small peaks are discernible in each trace in Fig. 2(a). The overall structure is reminiscent of recent experiments on the tetralayer graphene that show multiple peak structures [28-29].

To study the observed peak structure further, we measured the detailed response of the resistivity ρ to V_b and V_t . Figure 2 (b) shows a map of resistivity as a function of V_b and V_t , which were measured at $B = 0$ T and $T = 4.2$ K. ρ shows a significant variation with the top and bottom gate voltages. The peak resistivity,

which is approximately on a straight line that passes through the origin is the trace of the main peak in Fig. 2(a), which is due to charge neutrality. In addition, a curved ridge structure, which looks like a set of hyperbolas, is discernible. Similar structures were observed in AB-stacked tetralayer graphene [28-29].

Applying gate voltages to the top and bottom gate electrodes allowed us to control the perpendicular electric fields and carrier density independently. The top gate voltage V_t induces charges, $-en_t (= C_{tg} V_t)$, in the graphene, while the back gate voltage V_b induces charges, $-en_b (= C_{bg} V_b)$. Here, C_{tg} and C_{bg} are the specific capacitances of the top and bottom gate electrodes, respectively. The total carrier density n_{tot} is the sum, $-e n_{tot} = C_{tg} V_t + C_{bg} V_b$. Here, the electric flux density perpendicular to the sample is given by $D_{\perp} = -(C_{tg} V_t - C_{bg} V_b)/e$. Therefore, the condition for constant D_{\perp} can be attained by varying the top and bottom gate voltages to satisfy the condition, $V_t = C_{tg}/C_{bg} V_b + V_0$, where $D_{\perp} = -C_{bg}V_0/e$. On the other hand $n_{tot} = 0$ at the conspicuous ridge structure for the charge neutrality in Fig. 2(b), so that the top gate and bottom gate voltage satisfy the condition, $C_{tg}\Delta V_t = -C_{bg}\Delta V_b$. This gives the ratio of the capacitances, $C_{tg}/C_{bg} \approx 7$.

Figure 2 (c) shows a replot of Fig.2 (b) as a function of total carrier density n_{tot} and $-eD_{\perp}$. The ridge structure for charge neutrality is vertically elongated at $n_{tot} = 0$. In addition, hyperbolic ridges appear symmetrically in $-eD_{\perp}$.

Landau level structures

Before studying the structure of the resistance ridge, we studied the Landau level structure, from which we could deduce the low-energy band structures at a zero magnetic field. The magnetoresistance was measured as a function of the top and bottom gate voltages. The top and bottom gate voltages were varied to keep a condition of $D_{\perp} = 0$ to minimize the internal graphene potential induced by the gate voltages. Figure 3 (a) shows a map of longitudinal resistivity ρ_{xx} as a function of n_{tot} and magnetic field B . Shubunikov-de Haas (S-dH) oscillations manifest

themselves as bright and dark patterns. Unlike mono- and bilayer graphene [1], the Landau levels are not simple fan-shaped structures, but possibly consist of overlaid fan-shaped structures that have complicated level crossings [20-24,28-29,44]. This complexity arises from the fact that the low-energy band structure of the AB-stacked hexlayer graphene consists of three bilayer bands [5,7-10,24,45].

One of the most characteristic features in Fig. 3 (a) is the emergence of zero-mode Landau levels, α , β , and γ , which are located near the charge neutrality point. Each of these zero modes remains approximately at the same value of n_{tot} as B increases. The degeneracy of the zero-mode Landau levels is a clue to determining the nature of each band. The degeneracy can be identified by inspecting the variation in the filling factors of the energy gaps associated with the Landau level crossings. Some of the energy gaps and filling factors are indicated on the Landau fan diagram in Fig. 3 (b). It is easy to verify that the zero-mode Landau levels α and γ have eight-fold degeneracy, which is a characteristic feature of bilayer-like bands [1,3,46-47]. The zero-mode Landau level α is between gaps with $\nu = -8$ and -16 at $B \approx 4$ T, and between -12 and -20 at $B \approx 3$ T. The zero-mode γ , on the other hand, is between gaps with 8 and 16 at about $B = 6$ T and between gaps with 12 and 20 at $B \approx 5$ T. (The relevant positions are indicated by horizontal lines.) The difference between the filling factors of the gap is eight, which is the degeneracy of the zero-mode Landau levels of the bilayer-like bands. This contrasts with the case of a monolayer-like band. The zero-mode Landau level has a degeneracy of four [1,20,23-24].

Comparison with calculation

To better understand the experimentally obtained fan diagram, we performed theoretical Landau level calculations. The Hamiltonian is based on the effective mass approximation of the tight binding model. Figure 3 (c) shows the energy eigenvalues of the Hamiltonian of AB-stacked hexlayer graphene in a magnetic field calculated for the Slonczewski-Weiss-McClure parameters of graphite, and Fig. 3(d) is a numerically calculated Landau fan diagram, which shows density of

state as a function of carrier density. Better agreement might be obtained by fine tuning of the SWMcC parameters; however, Fig. 3(d) nonetheless reproduces important features of the Landau fan diagram of AB-stacked hexlayer graphene. In particular, the presence of three zero-mode Landau levels with eight-fold degeneracy is readily seen as vertically elongated Landau levels. In Fig. 3 (a), although the zero-mode Landau levels α and γ are clearly related to the bilayer-like band, the degeneracy of the zero-mode Landau level β is not clear as a single level because of the large resistance that grows in the vicinity of $n_{tot}=0$ where β is expected to appear. As can be seen in Fig. 3 (c), near β , there is a four-fold degenerate Landau level that is electron-like above about $B > 3$ T. These two Landau levels were not resolved in the experiment and appeared between gaps with $\nu = -4$ and $+8$ in the high magnetic field regime. The fact that zero-mode Landau levels appeared at three different carrier densities shows the semi-metallic features of the hexlayer graphene, because zero-mode Landau levels appear at the bottoms of the conduction and valence bands. This indicates that as the number of layers increases, the graphene should become graphite, which is prototype semi-metal. It is clear that stacking of graphene is essential for the semi-metallic band structure to appear, because monolayer graphene does not have semi-metallic features at all. The dispersion relation in the direction of stacking is principally due to γ_2 of the SWMcC parameters, which represents the interlayer coupling [11,44].

The other important feature of the Landau fan diagram is the characteristic filling factor of the energy gap. An energy gap for a filling factor $\nu = -4$ is expected to appear between two zero-mode Landau levels, as seen in Fig. 3 (c). There is no Landau level crossing that close this energy gap above $B \sim 2.5$ T. In the experimental fan diagram, the energy gap with $\nu = -4$ appears as a resistance ditch structure. This kind of energy gap between zero-mode Landau levels forms characteristic energy-gap structures in the fan diagram in multilayer graphene. As another example, the gap with $\nu = 8$ is clearly visible near the charge neutrality point approximately above $B > 4$ T. The energy gap is located between the zero-

mode Landau levels β and γ . The filling factor of the gap is $\nu = 8$ (not $\nu = 4$), because an electron-like Landau level with a degeneracy of four exists between the zero-mode Landau levels β and γ .

Splitting of zero-mode and variation of energy spectra in presence of perpendicular electric field.

So far we have studied the Landau fan diagram for $D_{\perp} = 0$. Next, we examine the case of $D_{\perp} \neq 0$. Figure 4 (a) and (b) shows maps of longitudinal magnetoresistivity measured for $-eD_{\perp} = \pm 0.81 \times 10^{12} \text{ cm}^{-2}$. Here, top and bottom gate voltages were varied to investigate carrier density n_{tot} dependence of longitudinal resistivity while keeping D_{\perp} constant. It is clear that the zero-mode Landau levels split via the perpendicular electric field; the zero-mode Landau level γ in the electron regime splits into two levels, γ_1 and γ_2 , although the splitting is not clear in the hole regime. Splitting of zero-mode Landau levels of the bilayer-like band due to perpendicular electric fields also occurs in graphene with different numbers of layers [29-30,48].

Discussion

Now we return to the resistance ridge structures appearing in the gate voltage dependence at zero magnetic field, which is shown in Fig. 2 (b) and (c), and discuss it in the light of the electronic band structure of the AB-stacked hex-layer graphene. Fine structures are found in the derivative of resistivity with respect to n_{tot} , as shown in Fig. 5 (a). The ridge structures look similar to those of AB-stacked tetralayer graphene [28-29], in that ridges u and v cross. However the overall structure of the ridges is much more complicated than in the AB-stacked tetralayer graphene.

Some of the ridges are relevant to the bottoms of the bilayer-like band, which can be experimentally verified from the positions of the zero-mode Landau levels that appear. The positions of the zero-mode Landau levels indicated with red crosses in Fig. 5 (b), were experimentally measured for different values of $-eD_{\perp}$. As in the

case of AB-stacked tetralayer graphene [29], the positions are approximately on the ridges labeled u, v, and z. Since the zero-mode Landau levels are expected to appear at the bottoms of the band, it is naturally expected that the observed ridge structures u, v, and z originate from the positions of the bottoms of the bilayer-like bands. The crossing of ridges u and v would be due to splitting of the zero-mode Landau levels. At $D_{\perp} = 0$, there is no energy gap at the bottoms of the bilayer-like bands, and the perpendicular electric field opens up an energy gap.

If the crossing arises from the band structure, n_{tot} for the crossing point should differ between AB-stacked hexlayer and tetralayer graphene. In AB-stacked hexlayer graphene, the crossing occurs at $n_{tot} \sim 1.4 \times 10^{12} \text{ cm}^2$, while in tetralayer graphene, the crossing occurs at a smaller value, $n_{tot} \sim 0.9 \times 10^{12} \text{ cm}^2$ [29]. In the hole regime, the crossing feature of the ridge is not visible, nor it is the splitting of the zero-mode Landau levels. However, a zero-mode Landau level appears at $n_{tot} \sim -1.0 \times 10^{12} \text{ cm}^2$ in the hexlayer graphene, and at $n_{tot} = -0.8 \times 10^{12} \text{ cm}^2$ in the tetralayer graphene.

Other ridges that are clearly visible in Fig. 5(a), *i.e.*, w, x and y, were not observed in the results for AB-stacked tetralayer graphene. The above discussion based on the zero-mode Landau levels could not explain these ridges. However, as shown below, they also originate from the band structure of graphene. We analyzed the experimental results with the help of a numerical calculation of the dispersion relation. Figure 5 (c) shows the numerically calculated dispersion relation as a function of wave number along the x -direction (k_x), under the condition $k_y = 0$. The Slonczewski-Weiss-McClure (SWMcC) parameters of graphite were used in the calculation, the same as those to make the Figs. 3 (c) and (d). The dispersion relation at zero perpendicular electric field is rather complex, because complicated energy gaps formed by mixing of bilayer-like bands and by trigonal warping (as Fig. 6(b) shows, the dispersion relations become slightly simpler without the trigonal warping).

Some of the characteristic positions in the dispersion relations are labeled a-f and Δ_1 in Fig. 5 (c). The carrier densities at the characteristic positions of the band structures were numerically calculated from the area of the Fermi surface, which was calculated from the energy-contour of the dispersion relations. In Fig. 5 (b), the numerically calculated n_{tot} for the characteristic positions in the dispersion

relation, a-f and Δ_1 are plotted for different values of $|eD_{\perp}|$. Note that a finer determination of the SWMcC parameter would result in a better fitting between the experimentally observed ridges and the calculation. Ridges u and v correspond to cases a and b. Ridges y and z correspond to cases e and f. These results are consistent with the measured positions of the zero-mode Landau levels. The ridge x seems to stem from case c. Cases c and d correspond to the bottoms of the bilayer-like band whose zero-mode Landau level appears in the vicinity of $n_{tot} = 0$. The trace for case d, on the other hand, is not clear, because it occurs the near $n_{tot} = 0$, where the change in resistance against $|n_{tot}|$ is large.

Ridge w is irrelevant to the bottoms of the bilayer-like band. It corresponds to case Δ_1 , at which the energy gap separating the two bilayer-like bands closes, and a mini-Dirac cone appears. In a two-dimensional plot of the dispersion relation, three identical mini-Dirac cones are formed for each K and K' valley. The mini-Dirac cones are expected to appear in trilayer graphene under a perpendicular electric field [49]. The present mini-Dirac cones in hexlayer graphene originate from the same mechanism as in trilayers in that trigonal warping locally closes the energy gap formed by the perpendicular electric field.

From the above, the dispersion relation in the presence of trigonal warping has complicated energy gap structure, as shown in Fig. 5 (c). It would be useful to examine the case of a simplified band structure without trigonal warping. Figure 6 (a) shows the dispersion relation calculated for the same SWMcC parameters, excepting that γ_3 and γ_4 are both set to zero. Here let us examine the positions in the band labelled a-f and Δ_1 - Δ_4 . The dispersion relations are isotropic with respect to the direction of the wave vector. By applying a perpendicular electric field, energy gaps appear at the bottoms of the bilayer-like band. In addition, there are energy gaps between different sets of bilayer-like bands, for example, energy gaps between Δ_1 and Δ_2 and between Δ_3 and Δ_4 . The carrier densities at positions a-f and Δ_1 - Δ_4 were numerically calculated, and the results are overlaid on the experimental data as shown in Fig. 6 (b). The traces for a-f explain the experimentally observed ridge structures u, v, x, y, and z. On the other hand, the traces for Δ_1 and Δ_2 are approximately on ridge w, which corresponds to the case of Δ_1 in Fig. 5 (c), where Dirac points for the mini-Dirac cones are expected to appear. The mini-Dirac cone is originally due to the gap between Δ_1 and Δ_2 closing in Fig. 6 (a), so that they would appear at approximately the same

positions. The traces for Δ_3 and Δ_4 in Fig. 6 (b) appear between traces e and d. This would explain the weak ridge structure between ridge y and the ridge at $n_{tot} = 0$ (*i.e.*, the weak ridge between ridge e and d in Fig. 5(b)). This ridge would correspond to the hole-version of ridge w in the electron region.

The band structure of graphene becomes more complicated as the number of layers increases, and accordingly, the band mass varies complicatedly in the reciprocal space. Phenomena due to this complication should appear in the resistivity measured at zero-magnetic field for sufficiently high-quality samples. In addition to the Shubnikov-de Haas effect due to Landau quantization in the magnetic field, a detailed measurement of resistivity at zero magnetic field would be a powerful and complementary method for studying the electronic band structures by using transport measurements.

Conclusion

Low-energy electronic bands of AB-stacked hexlayer graphene were measured by using samples with top and bottom gate electrodes to control the perpendicular electric field for creating an internal electrostatic potential in graphene. Low-temperature magnetoresistance measurements showed clear Shubnikov-de Haas oscillations. The Landau fan diagram revealed that the six-layer graphene consists of three sets of bilayer-like bands. The Landau level structure is significantly influenced by the perpendicular electric field. In particular, splitting of the zero-mode Landau level is clearly observed, which in turn implies formation of an energy gap at the bottom of the bilayer-like band. In addition, the zero-field resistivity showed a significant variation due to the perpendicular electric field. Ridge structures were observed in the map of resistivity as a function of the total carrier density and perpendicular electric field, as have been observed in Bernal-stacked tetralayer graphene. Some of the ridge structures appeared at the same positions on the map, which indicates that the structures originate from the bottoms of the conduction and valence bands of the split bilayer-like band. We also detected a possible mini-Dirac cone in the perpendicular electric field.

Appendix:

1. Sample Fabrication

Graphene samples were prepared by mechanically exfoliating high-quality Kish graphite. A graphene flake was encapsulated with *h*-BN flakes prepared by using mechanical exfoliation of a high-quality *h*-BN crystal. The encapsulation technique is described in Ref. [43]. To make a dual-gated sample, the encapsulated graphene was formed on heavily doped Si substrate covered with SiO₂. The Si substrate remains conductive at $T = 4.2$ K, and hence serves as a bottom gate electrode. The top gate electrode was formed from a thick graphene flake, which was transferred onto the top of the encapsulated graphene by using the technique described in Ref. [20]. Samples were patterned into Halls bar by using electron beam lithography. Electric contacts to the graphene were made using the edge contact technique [43].

2. Determining the number of layers and stacking

The number of layers of graphene was determined by using various methods. After the mechanical exfoliation of the graphite, hexlayer graphene flakes were found by analyzing the color of the flakes [50-52]. The relationship between number of layers and the color of the graphene flakes was examined by measuring the thickness of the graphene flakes by using AFM topography. We also performed Raman spectroscopy using samples with a known number of layers. Raman G' peaks were measured for many graphene samples. Most of them revealed a systematic variation with the number of layers. There are reports on measuring the Raman G' peaks of AB-stacked graphene with 1-8 layers [24,53-58]. Figure 7 (a) shows the Raman G' spectra. Our data approximately reproduced the line shapes of the reported AB-stacked multilayer graphene. [53-58]. The Raman G-band spectra also showed a systematic enhancement with the number of layers as reported in Refs. [24,53,59]. Moreover, systematic variations appeared most frequently in flakes that were exfoliated from Kish graphite, which is consistent with that the samples are AB-stacked considering that AB-stacking is the most stable. We also found flakes

whose spectra were qualitatively different from the Raman G' band and whose stacking was possibly ABC [54-55].

There is a possibility that graphene flakes have domains with different stackings, despite that the number of layers is constant in the flake. In the previous studies, the stacking sequence was detected in a Raman mapping experiment examining the ratio of spectra intensities at two different Raman shifts in the G' band spectra [56,59]. We found that mapping the spectra intensity at a Raman shift near the Raman G peak clearly revealed differences in the stacking sequence [24]. We prepared many graphene flakes from graphite crystals supplied by different vendors. Flakes with ABC-stacking were found, though rarely in some batch of graphite crystal. In other batches, ABC stacking was not found at all.

We could not perform Raman spectroscopy on the samples used in the experiment, because they consisted of encapsulated graphene with a top gate of thick graphene. That is, a Raman measurement could not be performed on hexlayer graphene underneath a thick top gate graphene. Also, a Raman mapping experiment would have been difficult to perform during the sample fabrication process used in our laboratory because it could contaminate the surface of the sample. Moreover, the thick top gate insulator (a *h*-BN flake) to prevent leakage current from the top gate made it impossible to perform the Raman spectroscopy on the hexlayer graphene beneath the thick gate insulator.

For the above reasons, we performed similar experiments using other hexlayer graphene samples that had only a back gate electrode. If the Landau level structure of such a sample approximately reproduced the magneto transport results in the main text, it would confirm that the sample described in the main text was AB stacked six-layer graphene. Although graphene was also encapsulated with *h*-BN flakes in the back gate sample, the top *h*-BN flake was much thinner compared with the sample with the dual gate electrode, which enabled us to perform Raman spectroscopy. A map of the Raman G peak signal did not show any

significant variation in stacking in the sample, as shown in Fig. 7(b). The shapes of the Raman G' spectrum was approximately the same as that of AB stacked hexlayer graphene displayed in Fig. 7 (a) (see Fig 7 (c)) [54-56]. A map of magneto resistivity for this hexlayer graphene sample measured at $T = 4.2$ K is displayed in Fig. 8 (a). Figure 8 (b) compares the positions of the characteristic energy gaps between the back gate sample and the sample described in the main text. The Landau fan diagrams have approximately the same structure, which proves that the number of layers and stacking were the same [24].

3. Calculation of Landau levels

The Landau levels were calculated using an effective mass approximation based on the tight-binding model [44]. We used a Hamiltonian considering all the SWMcC parameters, *i.e.*, $\gamma_0, \gamma_1, \gamma_2, \gamma_3, \gamma_4, \gamma_5$ and Δ' [44]. Here, $\Delta' = \Delta - \gamma_2 + \gamma_5$. The definitions of the SWMcC parameters are depicted in Fig. 9. The wave functions were expanded using Landau functions [44], and the eigenvalues were calculated numerically. Because the crystal structure of AB-stacked six-layer graphene has spatial reversal symmetry, the Landau levels for K and K' valleys are degenerated. The density of states was calculated by assuming that each Landau level had a Gaussian distribution in energy with widths proportional to the magnetic field.

4. Calculation of dispersion relation

The dispersion relations were calculated using the Hamiltonian derived for the effective mass approximation [5,7-8,45]. The wave functions were expressed as the plane waves, and the eigen values of the matrix elements were calculated numerically. The effect of the perpendicular electric field was taken into account by adding, to the diagonal elements of the Hamiltonian, the electrostatic potential arising from the charge distribution due to the top and bottom gate voltages. The principle of inducing charges in graphene is approximately the same as a capacitor consisting of two metal gate electrodes to which a voltage is applied. However, although in a framework of classical electromagnetism, induced charges appear on the surface of each electrode, one must consider the distribution of the induced

charge within the graphene layers because graphene is an extremely thin material consisting of atomic layers. It is commonly accepted that the screening length is about a few layers. [13,31,61-65]. In this study, we chose the permittivity of graphene to be $\epsilon/\epsilon_0 = 2$ and the screening length to be $\lambda = 0.43$ nm, which is approximately the same as the theoretical values [63], and used them to analyze our past experimental results [24].

If $-eD_{\perp} = 2en_g$, charges en_g and $-en_g$ are induced at the top and bottom gate electrodes, respectively. The charge distributions due to the top and bottom gate voltages were calculated independently, as shown in Fig. 10. Here, we assumed that sum of the induced charges $e(n_1 + n_2 + \dots + n_6)$ equals the charge en_g induced by the gate electrode. The charge distribution due to the top and bottom gate voltages was calculated by superposing the individual charge distributions. The electrostatic potential for each layer was calculated by solving the Poisson equation.

The carrier density was calculated from the area of the energy contours of the dispersion relations as a function of the two-dimensional wave number $\vec{k} = (k_x, k_y)$.

Acknowledgements

This work was supported by KAKENHI No.25107003 from MEXT Japan. We thank M. Koshino at Osaka University and R. Saito at Tohoku University for valuable discussions in the early stage of this work. We also thank Y. Iye at the University of Tokyo for providing us with high-quality graphite crystals.

Contributions

RY conceived the experiments. The samples were made by TN, and ST. Measurements were done by TH, ST, TH, RE, and TO. The high quality h-BN crystals were grown by KW and TT. TH and RY analyzed the data. TN and RY wrote the manuscript.

Figure Captions

Figure 1

Characterization of Bernal-stacked six-layer graphene.

(a) Simplified band structure of hexlayer graphene. (b) Schematic diagram of sample structure. A vertical cross-section is displayed. (c) Optical micrograph of a sample. Top-gate graphene covers over the region relevant to the measurement, except on the electric leads for the excitation and voltage probes. The bar shows 10 μm . TG means top gate. hBN means *h*-BN flake.

Figure 2

Top and bottom gate voltage dependence of resistivity.

(a) Bottom gate voltage (V_b) dependence of resistivity for different top gate voltages (V_t). V_t was varied from 5 to -5 V in 1V steps. $T = 4.2$ K. $B = 0$ T. (b) Map of resistivity at zero magnetic field as a function of top and bottom gate voltages. $T = 4.2$ K. (c) Replot of panel (b) as a function of n_{tot} and $-eD_{\perp}$, which is proportional to the perpendicular electric field.

Figure 3

Magneto-transport measurement.

(a) Map of longitudinal magnetoresistivity (ρ_{xx}) as a function of carrier density (n_{tot}) and magnetic field (B). D_{\perp} was kept at zero. Arrows α , β , and γ indicate the positions of the zero-mode Landau levels. $T = 4.2$ K. (b) Filling factors ν of some of energy gaps and Landau level crossings are shown on the map. The horizontal line is a guide for eye for the width of the zero-mode Landau levels. (c) Numerically calculated Landau levels for AB-stacked hexlayer graphene. SWMcC parameters of graphite were used ($\gamma_0 = 3.16$ eV, $\gamma_1 = 0.39$ eV, $\gamma_2 = -0.02$ eV, $\gamma_3 = 0.3$ eV, $\gamma_4 = 0.038$ eV, $\gamma_5 = 0.038$ eV, $\Delta' = \Delta - \gamma_2 + \gamma_5 = 0.037$ eV). (d) Numerically calculated density of states.

Figure 4

Landau fan diagrams in the presence of perpendicular electric fields.

Map of longitudinal magnetoresistivity for $-eD_{\perp} = -0.8 \times 10^{12} \text{ cm}^{-2}$ (a) and 0.8×10^{12} (b) as a function of n_{tot} and B . $T = 4.2 \text{ K}$.

Figure 5

Resistance ridge structure in n_{tot} and D_{\perp} dependence.

(a) Map of the derivative of resistivity with respect to n_{tot} as a function of n_{tot} and D_{\perp} . Some of the ridge structures are labeled (u-z). (b) The same map, plotting the positions of zero-mode Landau levels, which were observed in the experiment, are plotted with red crosses. The other symbols indicate points a-f, and Δ_1 in the dispersion relation (see panel(c)), which was numerically calculated from the area of the energy contour of the dispersion. Lines are guides for the eye. (c) The dispersion relation of AB-stacked hexlayer graphene for different values of $|eD_{\perp}|$, that were calculated numerically using the SWMcC parameters of graphite. Representative points in the dispersion relations are labeled a-f and Δ_1 .

Figure 6

Resistance ridge and band structure calculation without trigonal warping.

(a) Dispersion relations of AB-stacked hexlayer graphene for different values of $|eD_{\perp}|$, which were calculated numerically using SWMcC parameters of graphite excepting $\gamma_3 = 0$ and $\gamma_4 = 0$. Representative points in the band structure are labeled a-f and Δ_1 - Δ_4 . (b) Similar to Fig. 5 (c), but the results for a-f and Δ_1 - Δ_4 are overlaid on the experimentally determined map.

Figure 7

Raman spectra of Bernal stacked six-layer graphene.

(a) Raman G' spectra for Bernal-stacked 3-6 layer graphene whose number of layers was calibrated by using AFM. (b) Map of Raman G band signal for sample with a single gate electrode. (c) Raman spectra of the same sample.

Figure 8

Comparison of Landau fan diagrams.

(a) Map of magnetoresistance for the sample with only a back gate electrode. (b) Comparison of the positions of some of the energy gaps. The solid line indicates the positions of the energy gaps. Numbers are filling factors. The left panel is for the sample with a single gate electrode. Right panel is for the sample with the dual gate electrode described in the main text.

Figure 9

Definition of Slonczewski-Weis-McClure (SWMcC) parameters.

Open circles indicate carbon atoms at A-site in the honeycomb lattice. Filled circles indicate carbon atoms at B-site.

Figure 10

Screening of gate-induced carriers.

Schematic diagram of induced charges in each graphene layer due to gate voltage from top or back gate electrode. d is the interlayer distance of multilayer graphene. λ is the screening length. $\vec{E}_1, \vec{E}_2, \dots, \vec{E}_5$ are the electric fields between the adjacent layers.

References

- [1] K. S. Novoselov, A. K. Geim, S. V. Morozov, D. Jiang, M. I. Katsnelson, I. V. Grigorieva, S. V. Dubonos, and A. A. Firsov, *Nature* **438**, 197 (2005).
- [2] P. R. Wallace, *Phys. Rev.* **71**, 622 (1947).
- [3] N. H. Shon, and T. Ando, *J. Phys. Soc. Jpn.* **67**, 2421 (1998).
- [4] H. K. Min, and A. H. MacDonald, *Phys. Rev. B* **77**, 155416 (2008).
- [5] M. Koshino, and T. Ando, *Solid State Commun.* **149**, 1123 (2009).
- [6] S. Latil, and L. Henrard, *Phys. Rev. Lett.* **97**, 036803 (2006).
- [7] M. Koshino, and T. Ando, *Phys. Rev. B* **76**, 085425 (2007).
- [8] M. Koshino, and T. Ando, *Solid State Commun.* **149**, 1123 (2009).
- [9] M. Nakamura, and L. Hirasawa, *Phys. Rev. B* **77**, 045429 (2008).
- [10] F. Guinea, A. H. Castro, and N. M. R. Peres, *Solid State Commun.* **143**, 116 (2007).
- [11] B. Partoens, and F. M. Peeters, *Phys. Rev. B* **74**, 075404 (2006).
- [12] C. L. Lu, C. P. Chang, Y. C. Huang, R. B. Chen, and M. L. Lin, *Phys. Rev. B* **73**, 144427 (2006).
- [13] T. Ohta, A. Bostwick, J. L. McChesney, T. Seyller, K. Horn, and E. Rotenberg, *Phys. Rev. Lett.* **98**, 206802 (2007).
- [14] C. Coletti, S. Forti, A. Principi, K. V. Emtsev, A. A. Zakharov, K. M. Daniels, B. K. Daas, M. V. S. Chandrashekar, T. Ouisse, and D. Chaussende, *Phys. Rev. B* **88**, 155439 (2013).
- [15] Z. Q. Li, E. A. Henriksen, Z. Jiang, Z. Hao, M. C. Martin, P. Kim, H. L. Stormer, and D. N. Basov, *Phys. Rev. Lett.* **102**, 037403 (2009).
- [16] L. M. Zhang, Z. Q. Li, D. N. Basov, M. M. Fogler, Z. Hao, and M. C. Martin, *Phys. Rev. B* **78**, 235408 (2008).
- [17] K. F. Mak, C. H. Lui, J. Shan, and T. F. Heinz, *Phys. Rev. Lett.* **102**, 256405 (2009).
- [18] K. F. Mak, J. Shan, and T. F. Heinz, *Phys. Rev. Lett.* **104**, 176404 (2010).
- [19] K. F. Mak, M. Y. Sfeir, J. A. Misewich, and T. F. Heinz, *Proc. Nat. Acad. Sci.* **107**, 14999 (2010).
- [20] T. Taychatanapat, K. Watanabe, T. Taniguchi, and P. Jarillo-Herrero, *Nat. Phys.* **7**, 621 (2011).
- [21] L. C. Campos, T. Taychatanapat, M. Serbyn, K. Surakitbovorn, K. Watanabe, T. Taniguchi, D. A. Abanin, and P. Jarillo-Herrero, *Phys. Rev. Lett.* **117**, 066601 (2016).
- [22] W. Z. Bao, Z. Zhao, H. Zhang, G. Liu, P. Kratz, L. Jing, J. Velasco, D. Smirnov, and C. N. Lau, *Phys. Rev. Lett.* **105**, 246601 (2010).
- [23] Y. Asakawa, S. Masubuchi, N. Inoue, S. Morikawa, K. Watanabe, T. Taniguchi, and

- T. Machida, Phys. Rev. Lett. **119**, 186802 (2017).
- [24] R. Yagi, T. Hirahara, R. Ebisuoka, T. Nakasuga, S. Tajima, K. Watanabe, and T. Taniguchi, Sci. Rep. Sci. Rep. **8** 13018 (2018).
- [25] A. L. Grushina, D. K. Ki, M. Koshino, A. A. Nicolet, C. Faugeras, E. McCann, M. Potemski, and A. F. Morpurgo, Nat. Commun. **6**, 6419 (2015).
- [26] Y. Nam, D. K. Ki, M. Koshino, E. McCann, and A. F. Morpurgo, 2D MATERIALS **3**, 045014 (2016).
- [27] Z. F. Wu, Y. Han, J. X. Z. Lin, W. Zhu, M. Q. He, S. G. Xu, X. L. Chen, H. H. Lu, W. G. Ye, and T. Y. Han, Phys. Rev. B **92**, 075408 (2015).
- [28] Y. M. Shi, S. Che, K. Zhou, S. P. Ge, Z. Q. Pi, T. Espiritu, T. Taniguchi, K. Watanabe, Y. Barlas, R. Lake and Lau, C. N. Lau, Phys. Rev. Lett. **120**, 096802 (2018).
- [29] T. Hirahara, R. Ebisuoka, T. Oka, T. Nakasuga, S. Tajima, K. Watanabe, T. Taniguchi and R. Yagi, be published in Sci. Rep.
- [30] T. Hirahara, R. Ebisuoka, K. Watanabe, T. Taniguchi, and R. Yagi, J. of Phys. Conf. Ser. **969**, 012150 (2018).
- [31] H. Miyazaki, S. Odaka, T. Sato, S. Tanaka, H. Goto, A. Kanda, K. Tsukagoshi, Y. Ootuka, and Y. Aoyagi, Appl. Phys. Express **1**, 034007 (2008).
- [32] L. Pietronero, S. Strassler, H. R. Zeller, and M. J. Rice, Phys. Rev. Lett. **41**, 763 (1978).
- [33] H. K. Min, B. Sahu, S. K. Banerjee, and A. H. MacDonald, Phys. Rev. B **75**, 155115 (2007).
- [34] E. V. Castro, K. S. Novoselov, S. V. Morozov, N. M. R. Peres, J. M. B. L. Dos Santos, J. Nilsson, F. Guinea, A. K. Geim, and A. H. Castro Neto, Phys. Rev. Lett. **99**, 216802 (2007).
- [35] A. A. Avetisyan, B. Partoens, and F. M. Peeters, Phys. Rev. B **80**, 195401 (2009).
- [36] A. A. Avetisyan, B. Partoens, and F. M. Peeters, Phys. Rev. B **79**, 035421 (2009).
- [37] M. Koshino, and E. McCann, Phys. Rev. B **79**, 125443 (2009).
- [38] T. Ohta, A. Bostwick, T. Seyller, K. Horn, and E. Rotenberg, Science **313**, 951 (2006).
- [39] A. A. Avetisyan, B. Partoens, and F. M. Peeters, Phys. Rev. B **81**, 115432 (2010).
- [40] S. H. Jhang, M. F. Craciun, S. Schmidmeier, S. Tokumitsu, S. Russo, M. Yamamoto, Y. Skourski, J. Wosnitza, S. Tarucha, and J. Eroms, Phys. Rev. B **84**, 161408 (2011).
- [41] K. Zou, F. Zhang, C. Capp, A. H. MacDonald, and J. Zhu, Nano Lett. **13**, 369 (2013).
- [42] W. Bao, L. Jing, J. Velasco, Y. Lee, G. Liu, D. Tran, B. Standley, M. Aykol, S. B. Cronin, D. Smirnov, M. Koshino, E. McCann, M. Bockrath, and C. N. Lau, Nat. Phys. **7**, 948 (2011).
- [43] L. Wang, I. Meric, P. Y. Huang, Q. Gao, Y. Gao, H. Tran, T. Taniguchi, K. Watanabe,

- L. M. Campos, and D. A. Muller, *Science* **342**, 614 (2013).
- [44] M. Koshino, and E. McCann, *Phys. Rev. B* **83**, 165443 (2011).
- [45] M. Koshino, and E. McCann, *Phys. Rev. B* **87**, 045420 (2013).
- [46] K. S. Novoselov, E. McCann, S. V. Morozov, V. I. Fal'ko, M. I. Katsnelson, U. Zeitler, D. Jiang, F. Schedin, and A. K. Geim, *Nat. Phys.* **2**, 177 (2006).
- [47] E. McCann, *Phys. Rev. B* **74**, 161403 (2006).
- [48] L. C. Campos, T. Taychatanapat, M. Serbyn, K. Surakitbovorn, K. Watanabe, T. Taniguchi, D. A. Abanin, and P. Jarillo-Herrero, *Phys. Rev. Lett.* **117**, 066601 (2016).
- [49] T. Morimoto, and M. Koshino, *Phys. Rev. B* **87**, 085424 (2013).
- [50] P. Blake, E. W. Hill, A. H. Castro Neto, K. S. Novoselov, D. Jiang, R. Yang, T. J. Booth, and A. K. Geim, *Appl. Phys. Lett.* **91**, 063124 (2007).
- [51] G. Q. Teo, H. M. Wang, Y. H. Wu, Z. B. Guo, J. Zhang, Z. H. Ni, and Z. X. Shen, *J. Appl. Phys.* **103**, 124302 (2008).
- [52] D. S. L. Abergel, A. Russell, and V.I. Fal'ko, *Appl. Phys. Lett.* **91**, 063125 (2007).
- [53] A. C. Ferrari, J. C. Meyer, V. Scardaci, C. Casiraghi, M. Lazzeri, F. Mauri, S. Piscanec, D. Jiang, K. S. Novoselov, and S. Roth, *Phys. Rev. Lett.* **97**, 187401 (2006).
- [54] C. X. Cong, T. Yu, K. Sato, J. Z. Shang, R. Saito, G. F. Dresselhaus, and M. S. Dresselhaus, *ACS NANO* **5**, 8760 (2011).
- [55] T. A. Nguyen, J. U. Lee, D. Yoon, and H. Cheong, *Sci. Rep.* **4**, 4630 (2014).
- [56] C. H. Lui, Z. Q. Li, Z. Y. Chen, P. V. Klimov, L. E. Brus, and T. F. Heinz, *Nano Lett.* **11**, 164 (2011).
- [57] A. C. Ferrari, and D. M. Basko, *Nat. Nanotechnol.* **8**, 235 (2013).
- [58] L. M. Malard, M. A. Pimenta, G. Dresselhaus, and M. S. Dresselhaus, *Phys. Rep.* **473**, 51 (2009).
- [59] A. Gupta, G. Chen, P. Joshi, S. Tadigadapa, and P. C. Eklund, *Nano Lett.* **6**, 2667 (2006).
- [60] D. Graf, F. Molitor, K. Ensslin, C. Stampfer, A. Jungen, C. Hierold, and L. Wirtz, *Nano Lett.* **7**, 238 (2007).
- [61] P. B. Visscher, and L. M. Falicov, *Phys. Rev. B* **3**, 2541 (1971).
- [62] F. Guinea, A. H. Castro Neto, and N. M. R. Peres, *Phys. Rev. B* **73**, 245426 (2006).
- [63] M. Koshino, *Phys. Rev. B* **81**, 125304 (2010).
- [64] N. J. Lee, J. W. Yoo, Y. J. Choi, C. J. Kang, D. Y. Jeon, D. C. Kim, S. Seo, and H. J. Chung, *Appl. Phys. Lett.* **95**, 222107 (2009).
- [65] D. P. Divincenzo, and E. J. Mele, *Phys. Rev. B* **29**, 1685 (1984).

Fig1

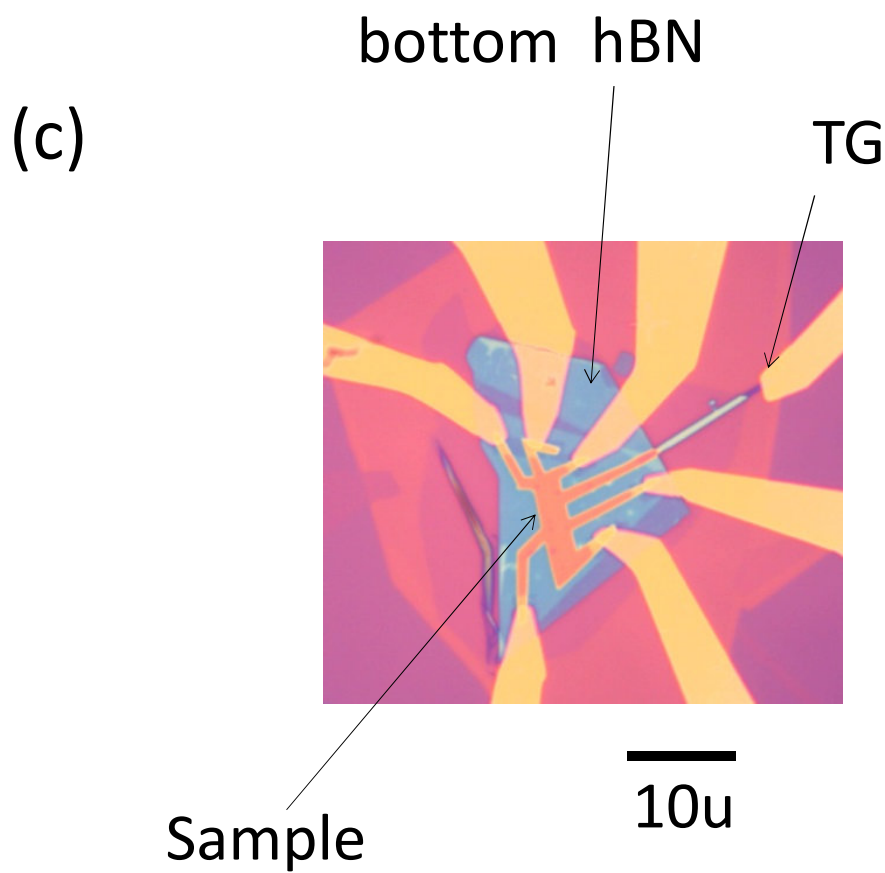
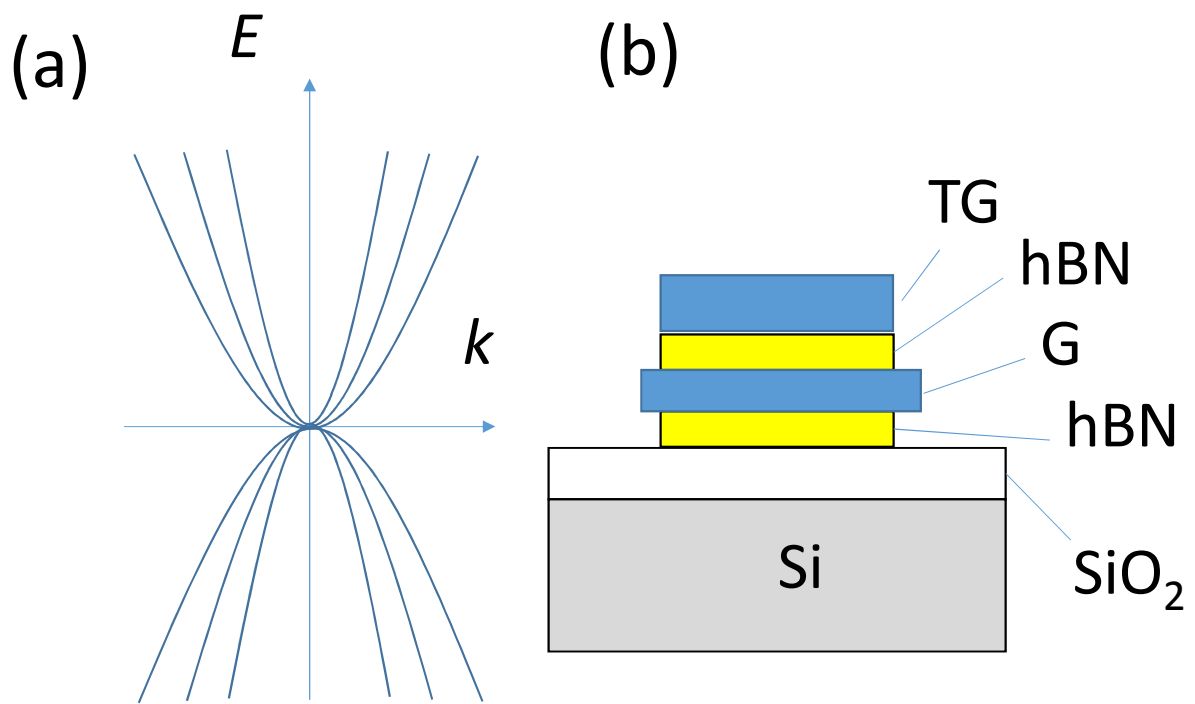


Fig2

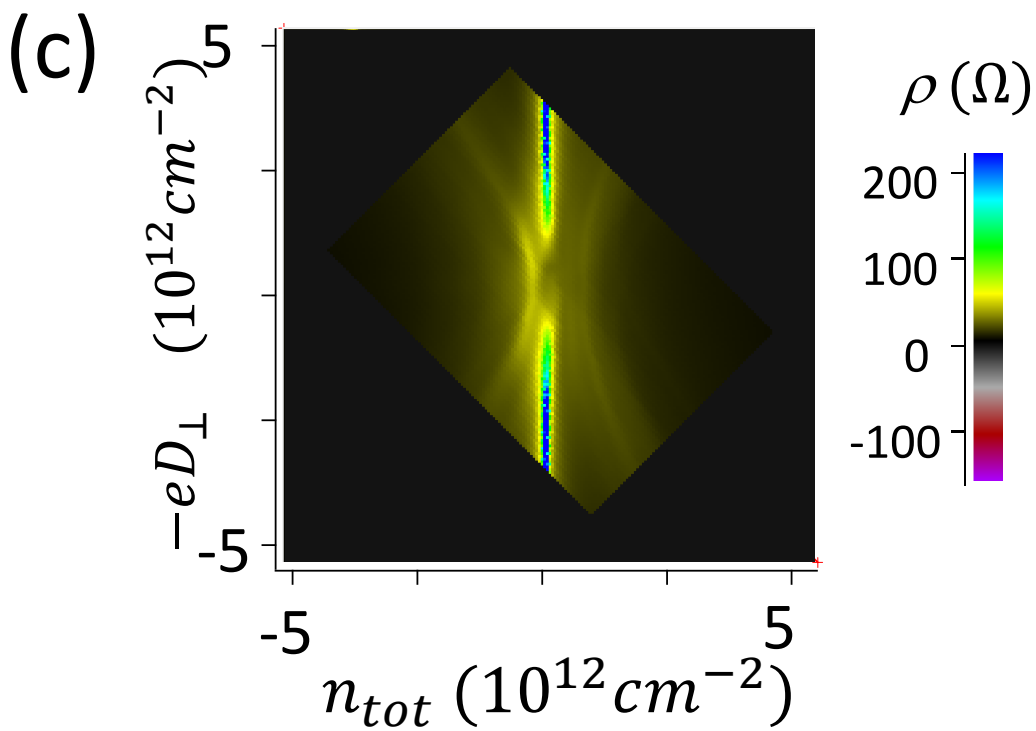
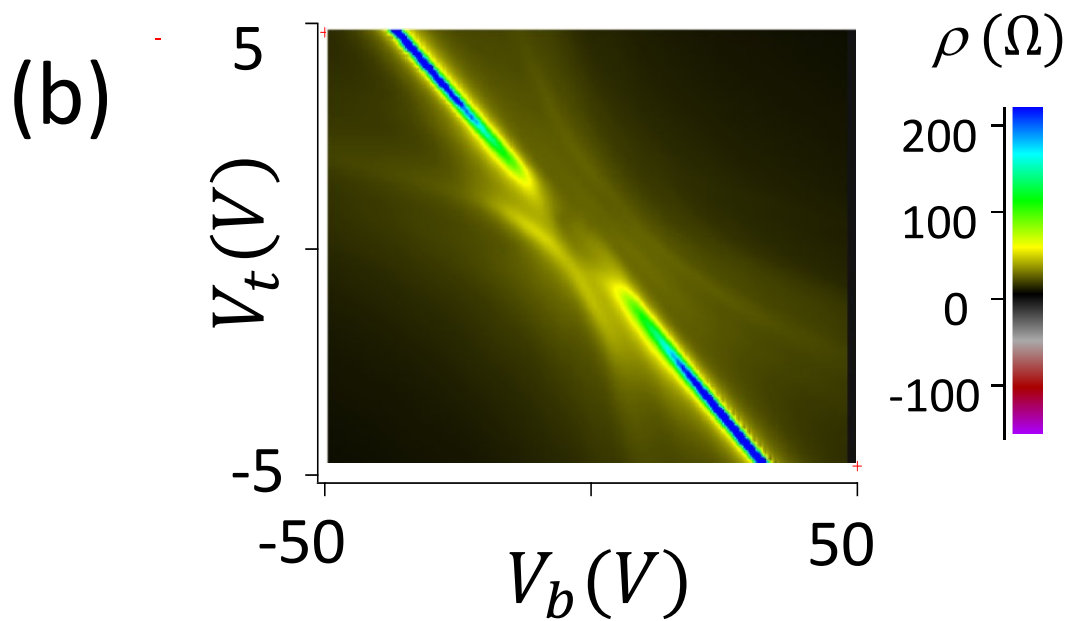
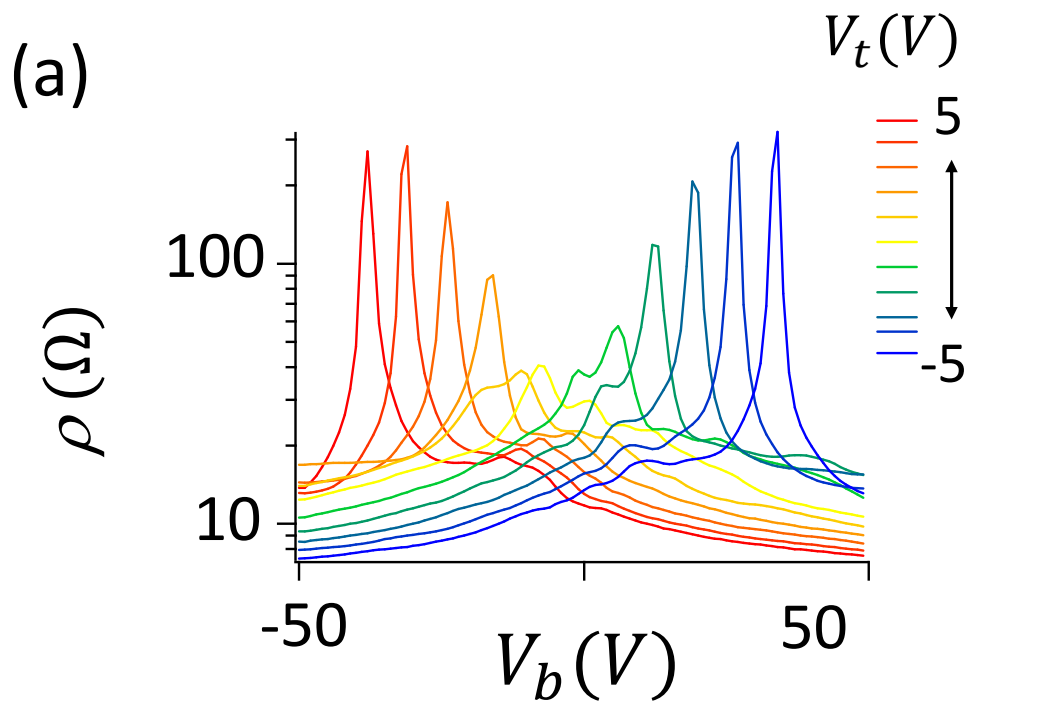


Fig 3

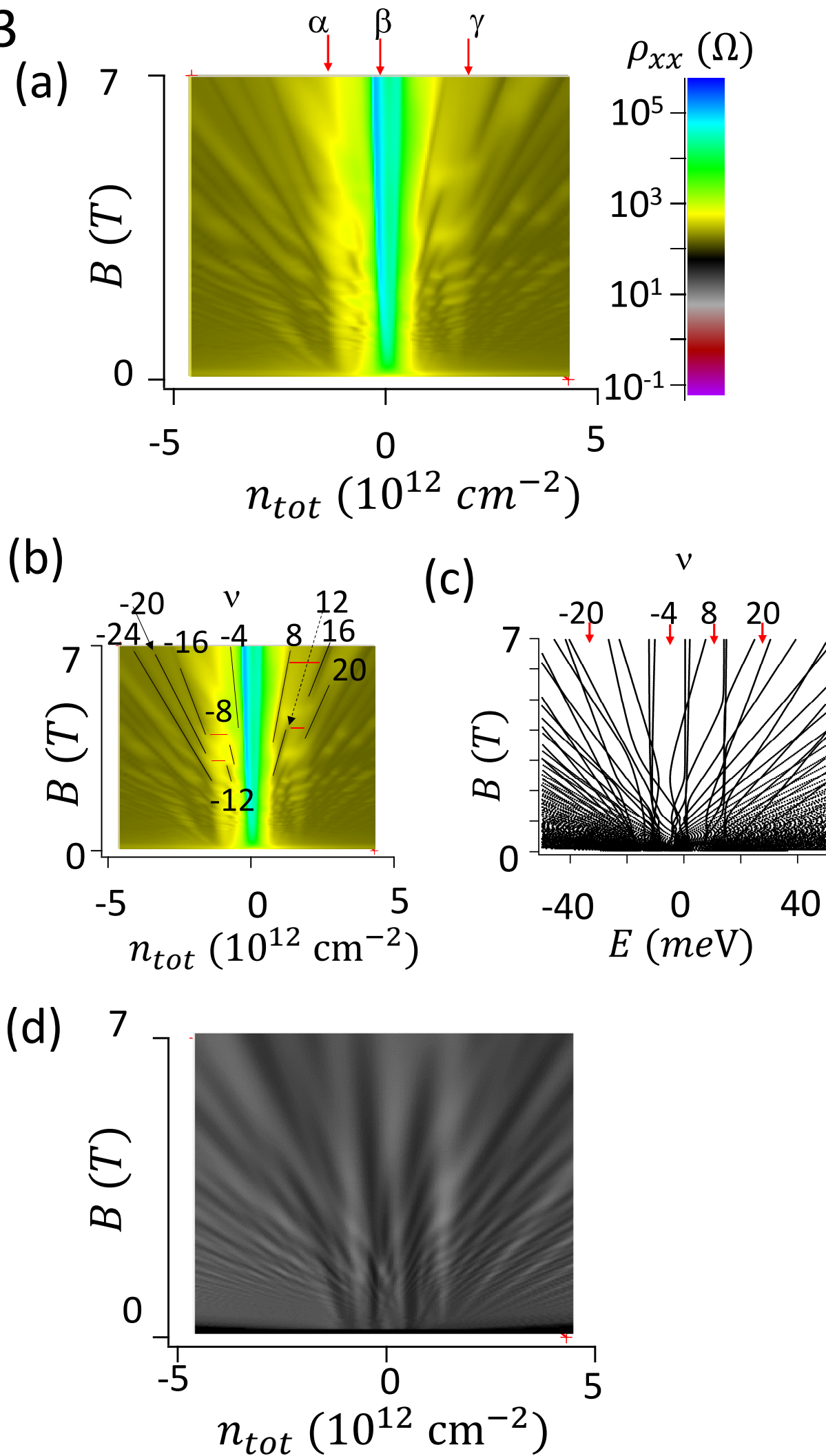
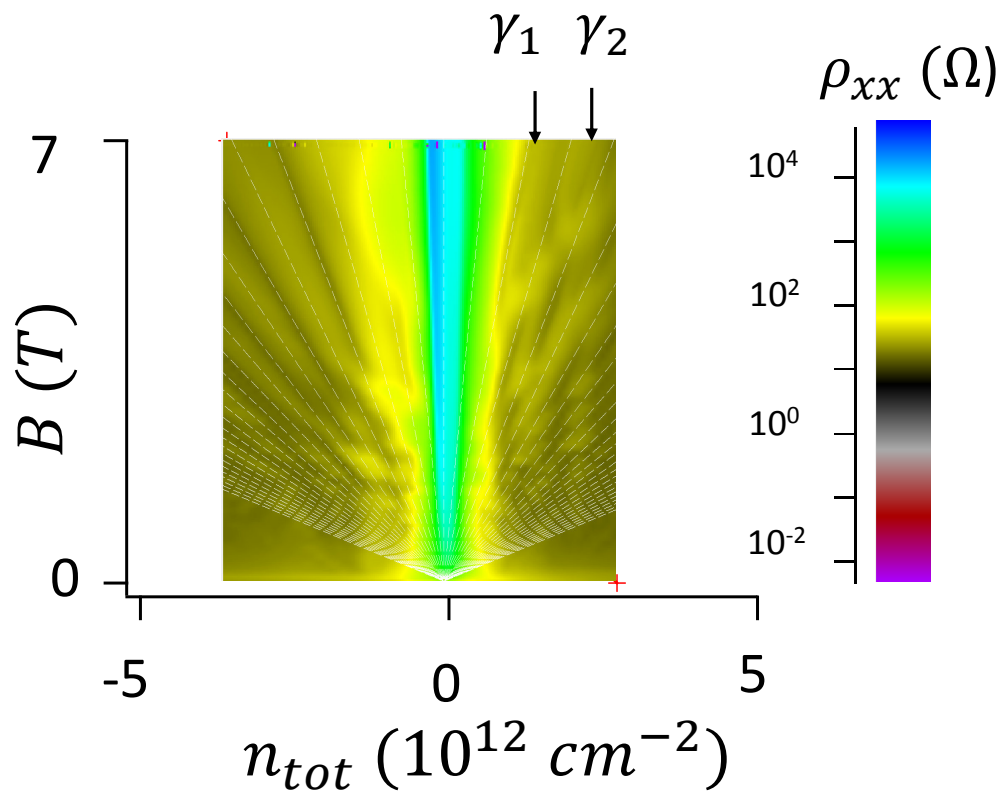


Fig. 4 (a) $-eD_{\perp} = -0.81 \times 10^{12} \text{ cm}^{-2}$



(b) $-eD_{\perp} = +0.81 \times 10^{12} \text{ cm}^{-2}$

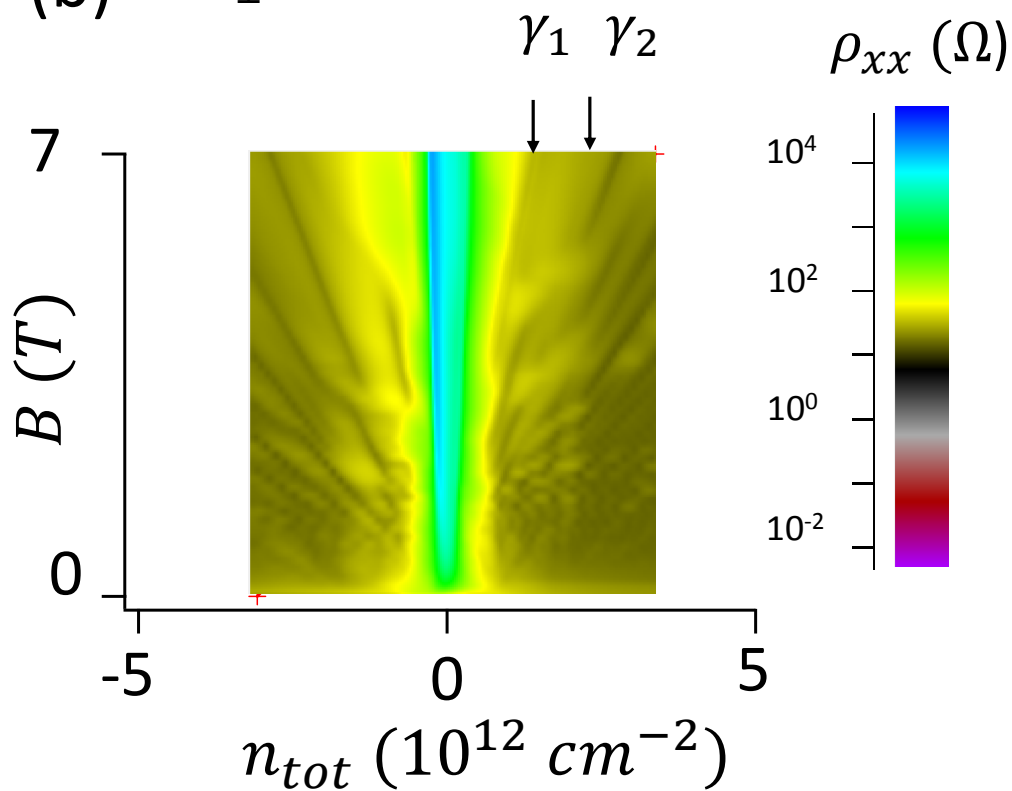


Fig. 5

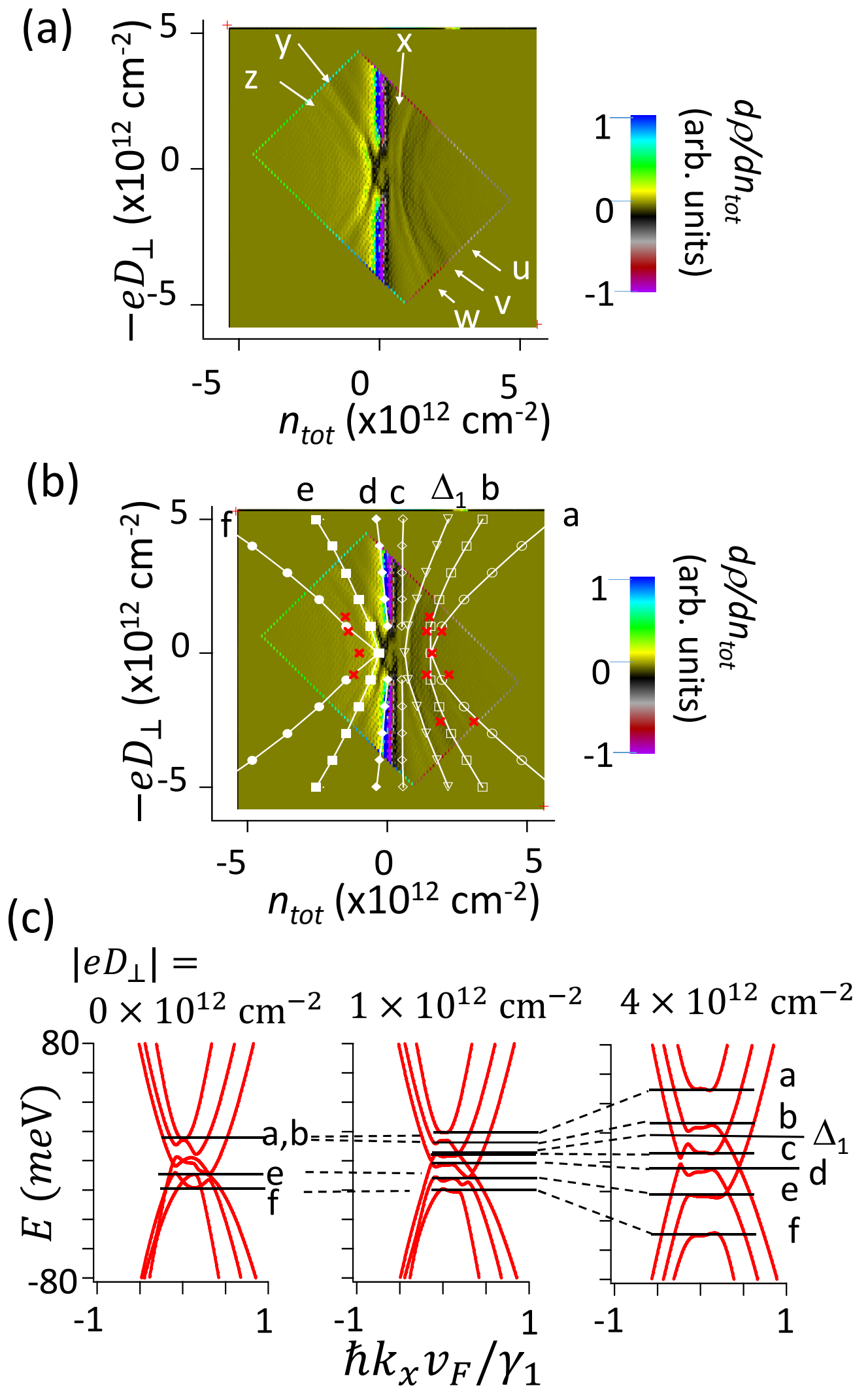


Fig. 6

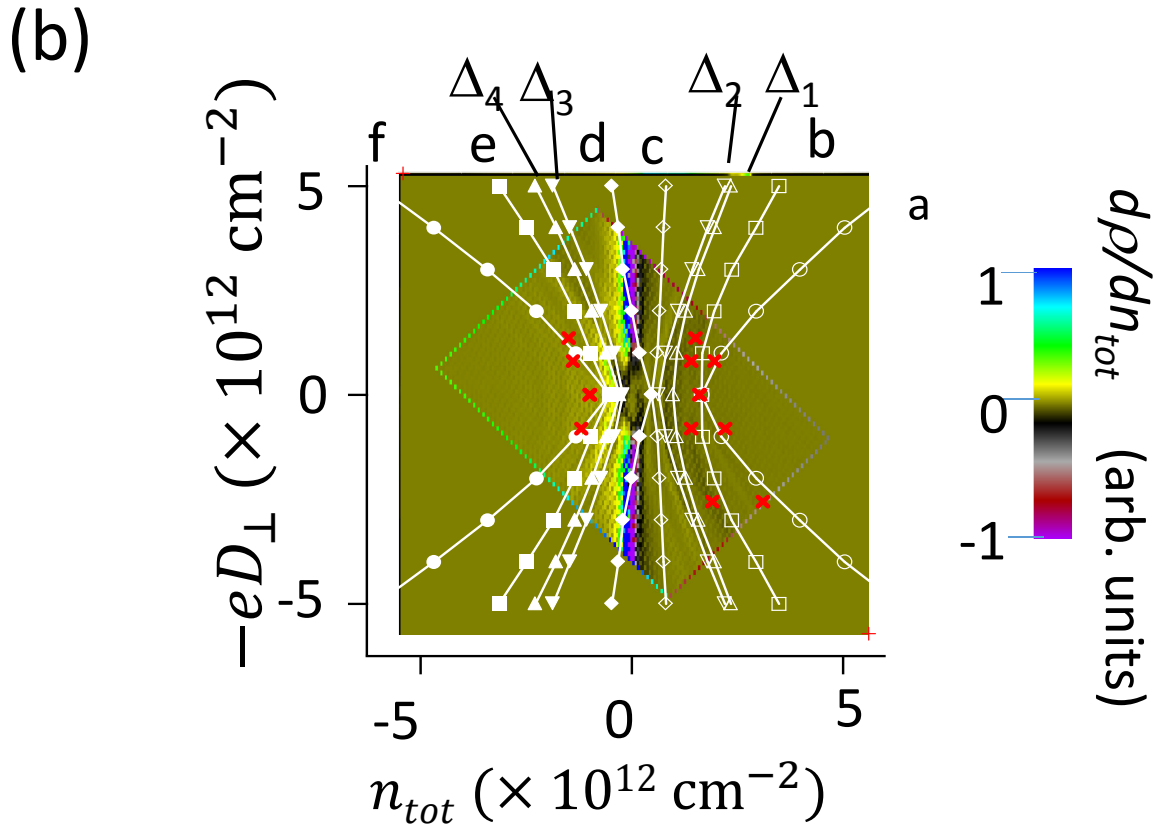
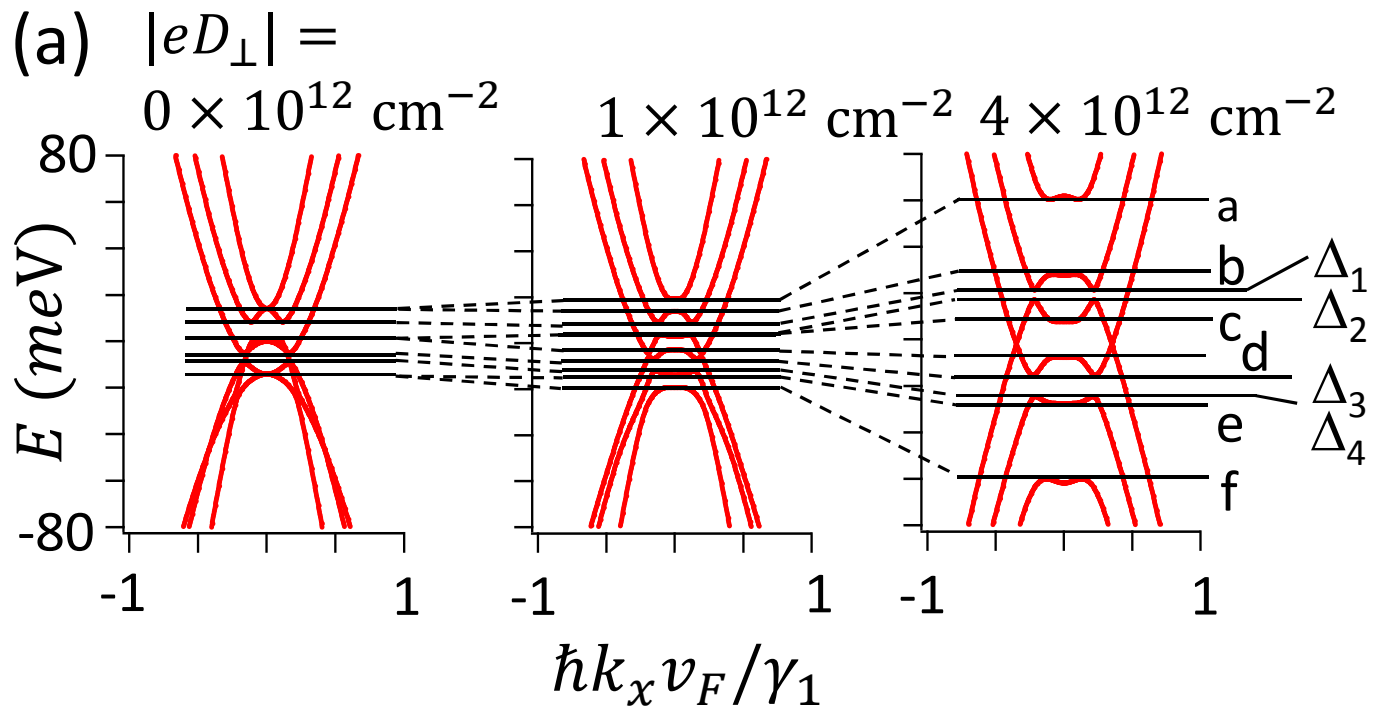


Fig. 7
(a)

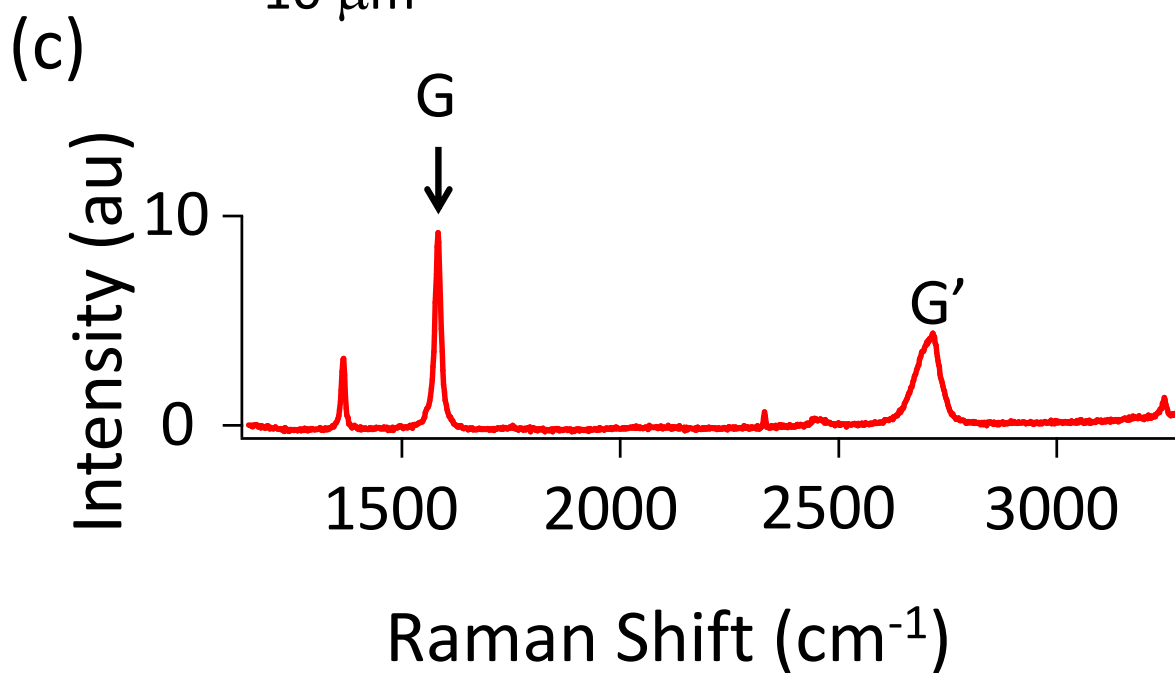
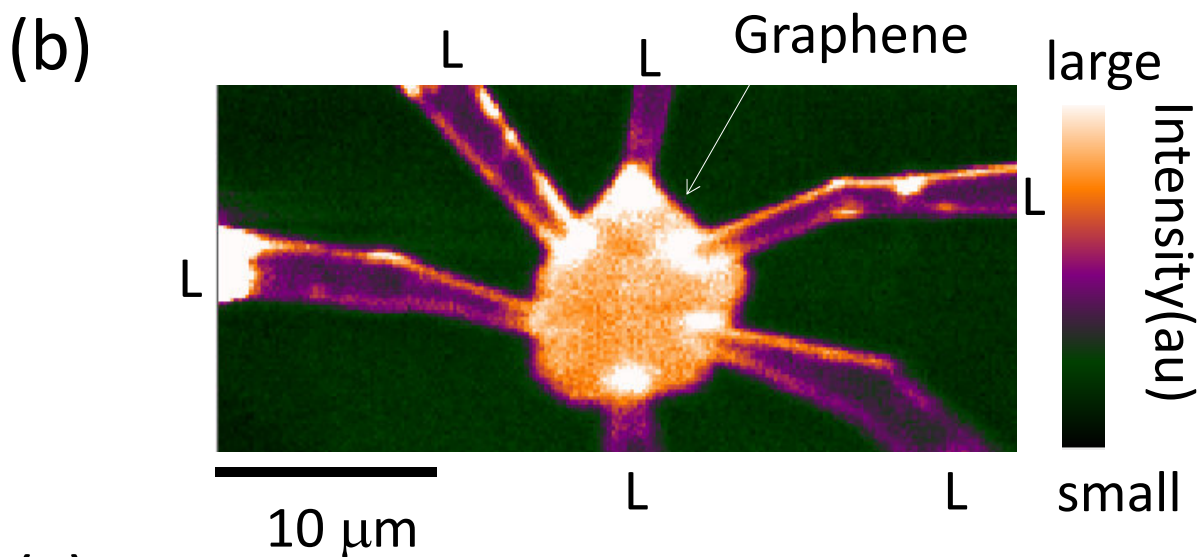
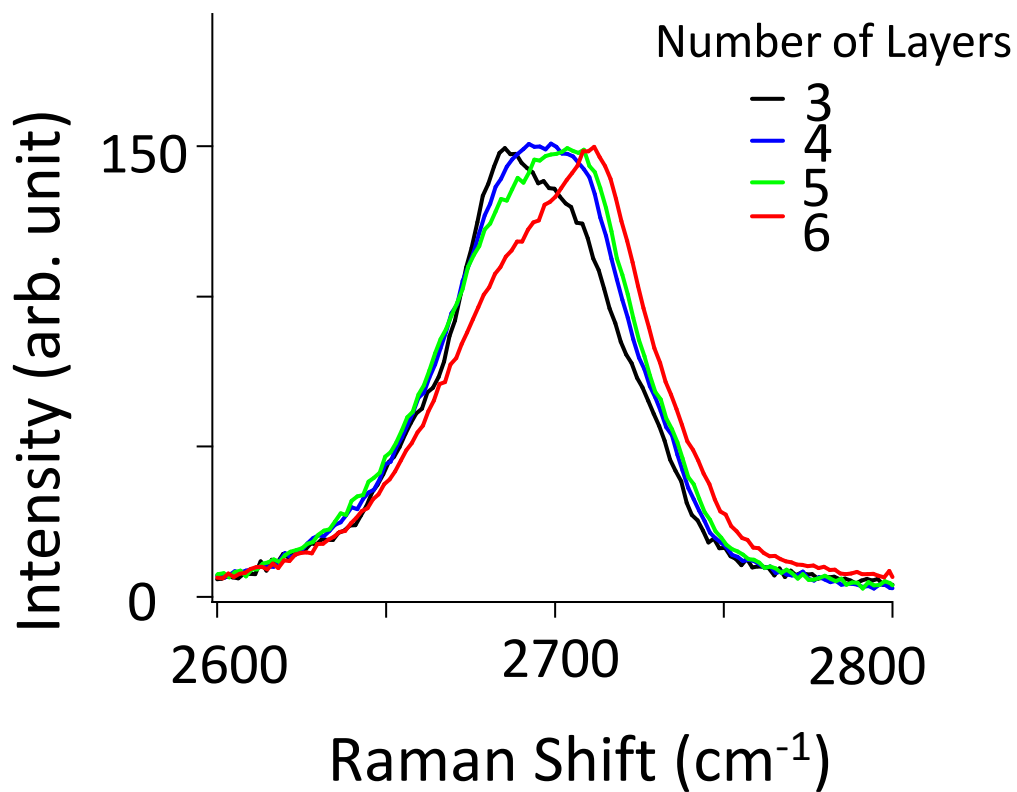


Fig. 8

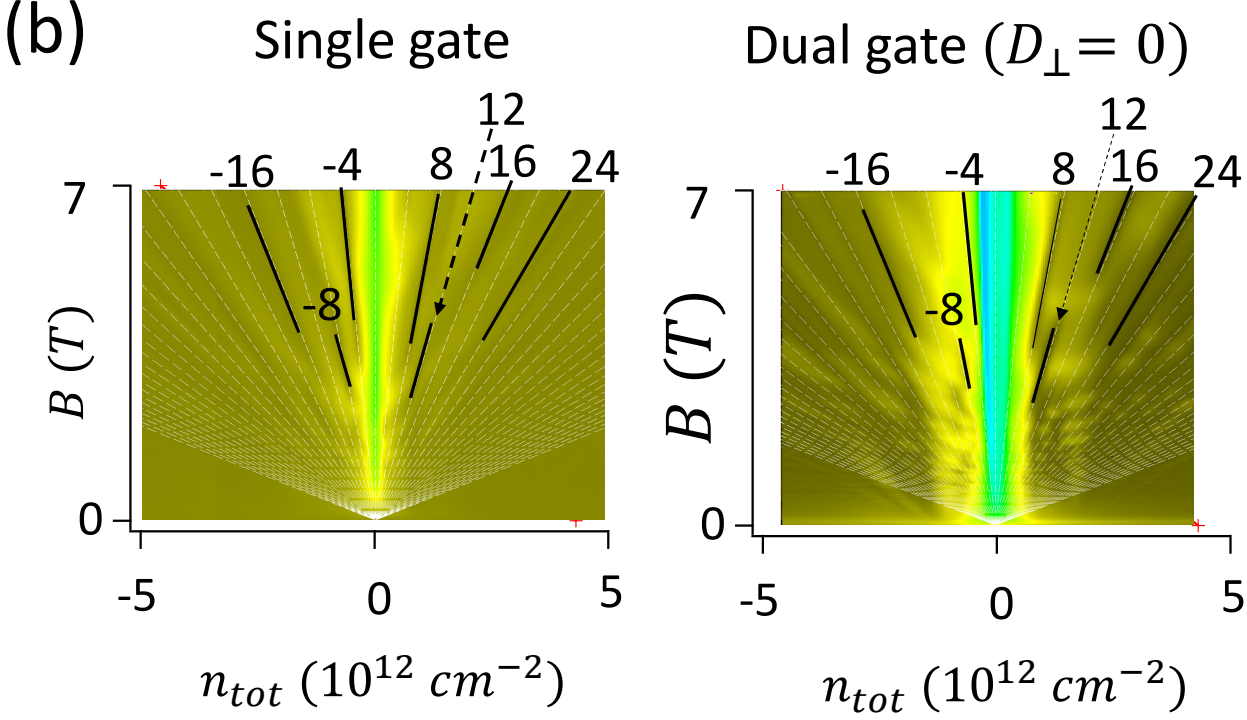
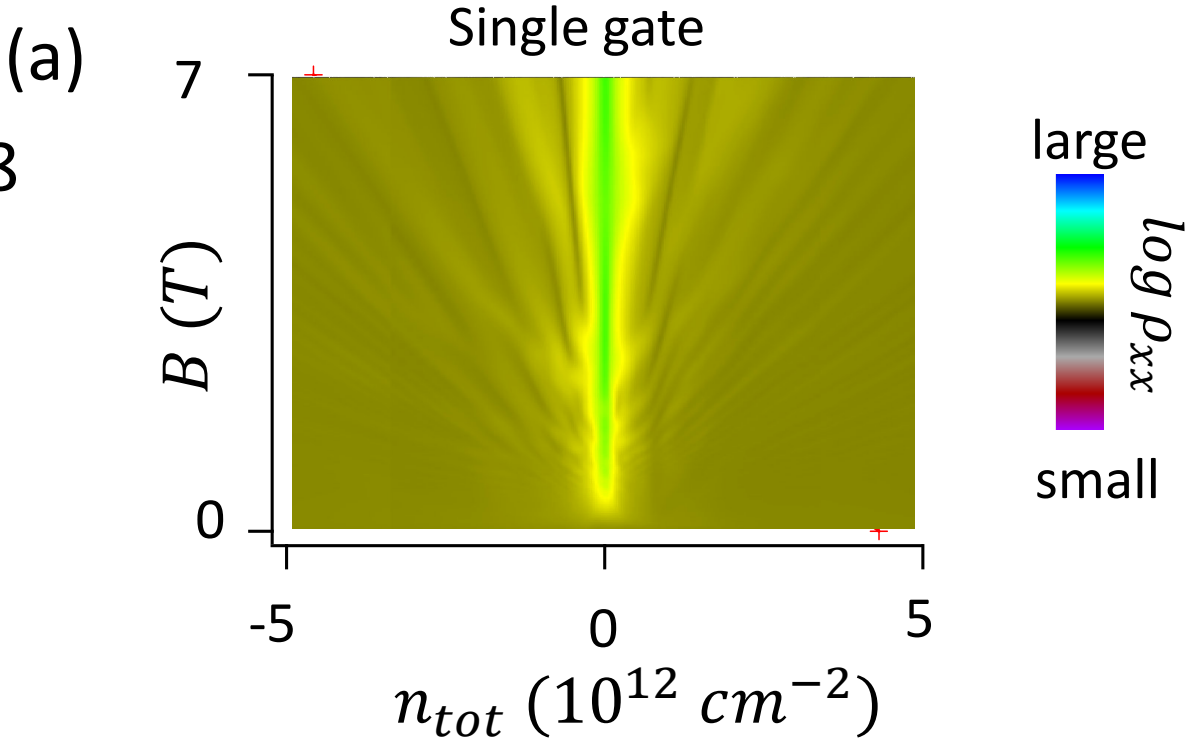


Fig. 9

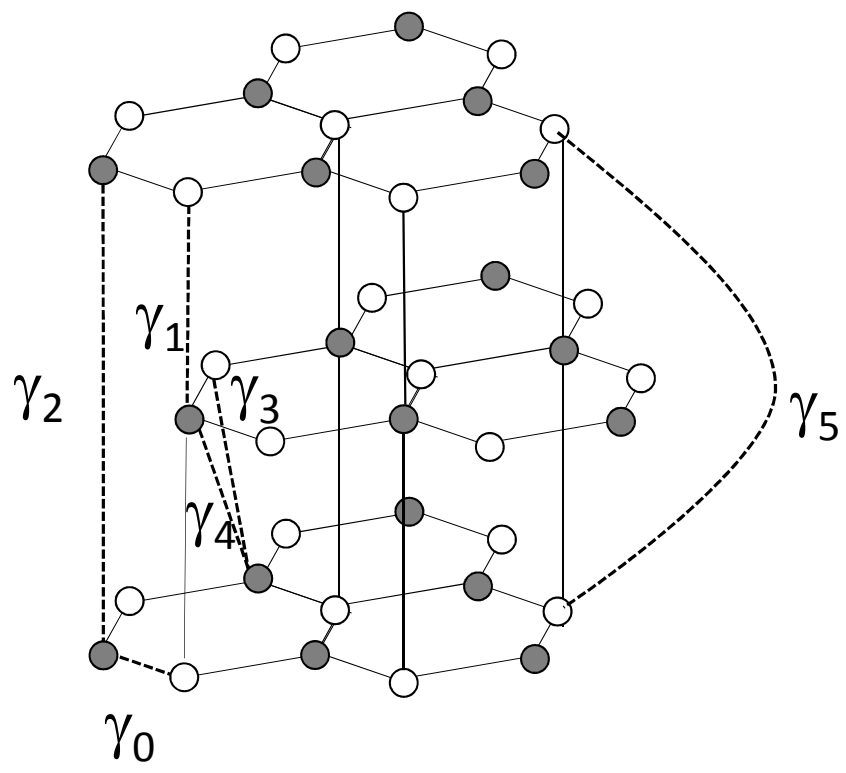


Fig. 9

